A novel forward-model technique for estimating EUV imaging performance - design and analysis of the SUVI telescope

Dennis Martínez-Galarce[a], James Harvey[b], Marilyn Bruner[c], James Lemen[a], Eric Gullikson[d], Regina Soufli[e], Evan Prast[f] and Shayna Khatri[f]

[a]Lockheed Martin Advanced Technology Center, Solar & Astrophysics Laboratory,
3251 Hanover Drive, Palo Alto, CA 94304;
[b]Center for Research and Education in Optics and Lasers (CREOL),
The University of Central Florida, Orlando, FL 32816;
[c]Bermar Science & Technology, 44 Roosevelt Circle, Palo Alto, CA 94306;
[d]Lawrence Berkeley National Laboratory, 1 Cyclotron Rd., Bldg. 2R0400, Berkeley, CA 94720;
[e]Lawrence Livermore National Laboratory, 7000 East Avenue, Livermore, CA 94550;
[f]L-3 Communications IOS-Tinsley, 4040 Lakeside Drive, Richmond, CA 94806

ABSTRACT

The Solar Ultraviolet Imager (SUVI) is one of several instruments being fabricated for use on board the upcoming Geostationary Operational Environmental Satellites, GOES-R and -S platforms, as part of NOAA's space weather monitoring fleet. SUVI is a Generalized Cassegrain telescope that employs multilayer coatings optimized to operate in six extreme ultraviolet (EUV) narrow bandpasses centered at 93.9, 131.2, 171.1, 195.1, 284.2 and 303.8 Å. Over the course of its operational lifetime SUVI will image and record full disk, EUV spectroheliograms approximately every few minutes, and telemeter the data to the ground for digital processing. This data will be useful to scientists and engineers wanting to better understand the effects of solar produced EUV radiation with the near-Earth environment. At the focus of the SUVI telescope is a thin, back-illuminated CCD sensor with 21 μm (2.5 arc sec) pixels. At the shortest EUV wavelengths, image degradation from mirror surface scatter effects due to residual optical fabrication errors dominate the effects of both diffraction and geometrical aberrations. Discussed herein, we present a novel forward model that incorporates: (*i*) application of a new unified surface scatter theory valid for moderately rough surfaces to predict the bi-directional reflectance distribution function (BRDF) produced by each mirror (which uses optical surface metrology to determine the power spectral density, PSD, that characterizes the "smoothness" of an optical surface); (*ii*) use of the BRDF for each mirror at each EUV wavelength, in tandem with the optical design, to calculate the in-band point spread function (PSF); (*iii*) use of the PSF to calculate the fractional ensquared energy in the focal plane of SUVI; (*iv*) comparison of BRDF measurements taken at 93.9 Å with the forward model predictions and (*v*) final prediction of the in-band, total system responsivity.

Keywords: SUVI, EUV solar physics, EUV optics, multilayer optics, BRDF of EUV optics, EUV optics surface scatter.

1. INTRODUCTION

The Geostationary Operational Environmental Satellites (GOES) are a fleet of satellites operated by the National Oceanic and Atmospheric Administration (NOAA) that are positioned in geostationary orbit to primarily observe the two oceanic coastal regions of the continental US. GOES provide near real-time monitoring of both the Earth and the near-Earth space environment to assist modelers and scientists to better understand and predict these environments. Because the GOES satellites lie fixed in orbit above the Earth surface, they provide a constant surveillance for atmospheric "triggers" of severe weather conditions that create tornadoes, flash floods, hail storms and hurricanes. And when these conditions develop, GOES are able to monitor storm development and track their movements. GOES are one of two types of satellites that NOAA uses for weather monitoring, and particularly, GOES serve as the short-range warning and "now-casting" system to alert NOAA's National Weather Service of impending severe weather conditions.[1]

The Solar Ultraviolet Imager (SUVI) is one of several instruments for the NOAA GOES "R" and subsequent missions. The SUVI optical system employs a generalized Cassegrain telescope consisting of multilayer coated optics, and a CCD detector at its focus to record images of the solar disk and its atmosphere in the extreme ultraviolet (EUV) regions of the spectrum. Using an aperture selector, SUVI operates at any one of six EUV narrow spectral passbands via combination of thin film filters and multilayer coated optics. Each optic (mirror) of the telescope has six distinct multilayer coatings that are fine-tuned to reflect at a well defined EUV wavelength that corresponds to a particular temperature region of the observed solar atmosphere. Five of the coatings use Mo/Si bilayers, while the sixth coating (for the shortest EUV wavelength) uses Mo/Y. The six multilayer coatings are designed to reflect at 9.4, 13.1, 17.1, 19.5, 28.4 and 30.4 nm. SUVI will image, record and telemeter spectroheliograms taken in the latter EUV passbands to observe the sun's atmosphere, composed of the chromosphere, transition region and corona. SUVI's main mission is thus to observe and record large energetic solar events, such as flares, coronal mass ejections and the solar wind, that affect Earth and its near-space environment, as well as to monitor the sun's long-term EUV production.

Figure 1 shows a representative sample of spectroheliograms recorded by EIT[2] (on board the ESA/NASA SoHO spacecraft) that are of similar image quality (5 x 5 arc sec[2]) to that which SUVI will return during its projected 15-year operational lifetime.
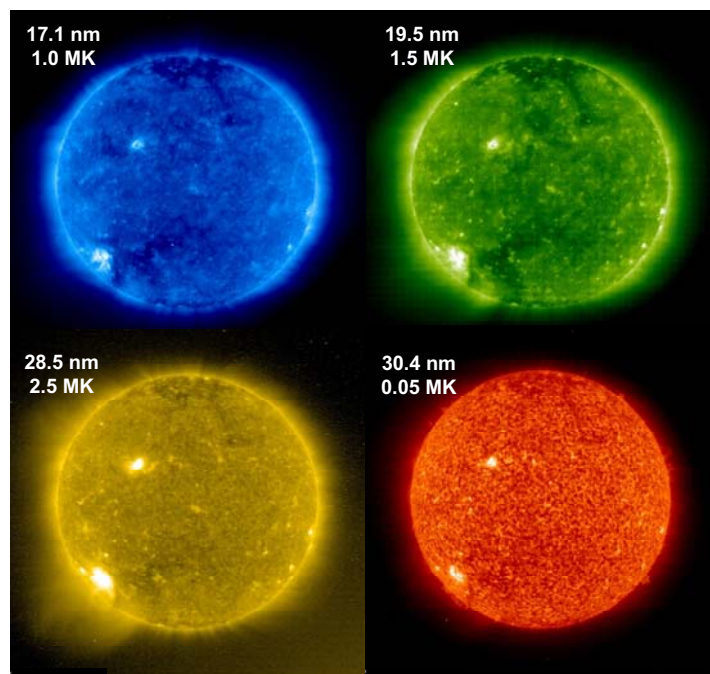

Figure 1. Shown above are representative EUV images (recorded by the EIT instrument on board SoHO) of four of SUVI's six EUV channels that will record spectroheliograms similarly to those shown. These images represent a discrete range of plasma temperatures of the sun's atmosphere, from ~50,000 K upto 2.5 x 10^6 K.

1.1 Calibration of EUV Instruments

EUV spectroheliographs composed of multilayer coated, normal incidence optics, were first flown on board sounding rocket instrument payloads beginning in 1987.[2-9] As detector technologies advanced and solar observations migrated from film-based, recording focal planes to electronic-based, charged-coupled devices (CCDs), EUV spectroheliographs have subsequently flown on board satellite based observatories that are fully dedicated to observing the sun. These observatories downlink spectroheliograms similar to those shown in Figure 1. SUVI, which will fly on board GOES-R and "-S" platforms, is the next-generation instrumentation of this important class of instruments that initially, was developed for use to study the EUV/soft X-ray solar atmosphere but now, is also used to study and monitor space weather. The accurate prediction of the in-band, EUV imaging performance of this class of instruments has at last come

within our ability to model and to accurately estimate. Herein, we present a forward model technique that uses both metrology data from optical surface characterization and modeling that is used to estimate EUV imaging performance of SUVI. This technique can be generalized for use of any EUV imaging instrument.

2. THE SUVI OPTICAL DESIGN

The SUVI telescope design is based on a generalized version of the Cassegrain configuration. A classic Cassegrain system consists of a concave parabolic primary mirror paired with a convex hyperbolic secondary mirror, as suggested in Figure 2. Parallel light from a point source at infinity is reflected toward the focus of the parabola. One focus of the hyperbola is placed at the focus of the parabola, which serves as a virtual source for the secondary mirror. Light reflected from the secondary mirror converges toward the other focus of the hyperbola, where it forms an aberration-free image on the optical axis. Principal aberrations at other field angles are coma, astigmatism and curvature of the field. A closely-related telescope type is the Ritchey-Chretien system, which employs a concave hyperboloid primary mirror coupled to a convex hyperboloid secondary mirror. The conic constants are adjusted such that both spherical aberration and coma are eliminated. It thus produces an aberration-free on-axis image with reduced small-field image degradation due to the absence of coma. The Ritchey-Chretien system still suffers from astigmatism and field curvature.
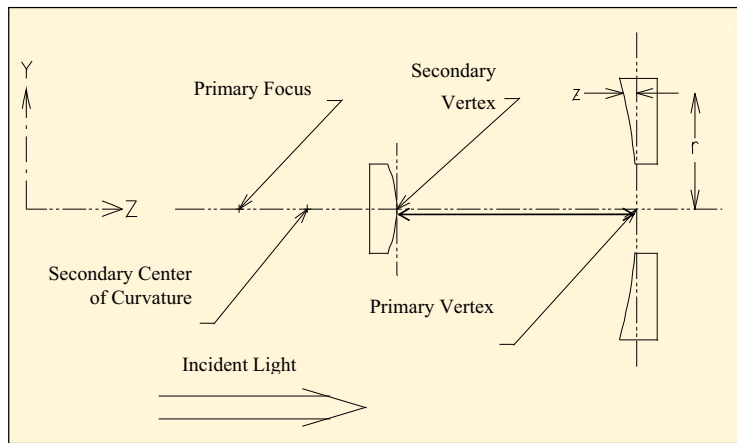

Figure 2. Schematic of SUVI optical system with a hyperbolic primary mirror and hyperbolic secondary mirror.

For the SUVI optical design, ray-trace optimization methods were used to balance the aberrations such that the geometrical image size was fairly uniform over the required flat field determined by the CCD detector. Two approaches were used, one beginning with a classical Cassegrain prescription and the other beginning with an equivalent Ritchey-Chretien prescription. Both gave essentially the same results. The optical prescription of this hyperboloid-hyperboloid generalized Cassegrain design is given in Table 1.

The most significant aberrations in the SUVI design are astigmatism and field curvature. Although the lower-order aberrations are nominally balanced, field curvature will introduce minor field-dependent distortions of the image that vary across the field. These may be important for observations requiring the accurate (i.e. ≈ 1 arc sec) location of compact sources. The optical design is diffraction limited (at visible wavelengths) where the core of the point spread function is less than one SUVI pixel (2.5 arc seconds).

The optical design also includes specifications for certain aperture masks and internal baffles that are required either for suppression of out-of-band radiation or to eliminate direct paths for particle radiation that might otherwise reach the CCD from non-solar origins. These items are not germane to the scattering discussion and will not be further discussed in this manuscript. Figure 3 shows the SUVI optical system to scale, together with a representative set of rays.

3. FORWARD-MODEL APPROACH TO ESTIMATE SUVI IMAGE PERFORMANCE

The analysis carried out and presented is only for the first SUVI flight mirror pair, called "Fx1" (composed of FP1 and FS1, which refer to the first flight primary and secondary mirrors, respectively). The Fx1 mirror pair has been designated for the engineering development unit (EDU) currently in production. Analyses performed for subsequent flight mirror pairs will be carried out in the exact same fashion as presented herein.

Figure 4 shows the flow of the forward model technique developed to estimate SUVI in-band imaging performance. In §4 we discuss each step of this forward model.

Table 1. SUVI Optical prescription.

Quantity	Value
Telescope type	Generalized Cassegrain
Primary Mirror diameter	20 cm
Primary mirror radius	138.62 cm
Primary mirror conic constant	-1.189743
Secondary mirror magnification	2.5
Secondary mirror radius	-91.10 cm
Secondary mirror conic constant	-7.698441
Vertex separation	42.00 cm
Back focal distance*	26.25 cm
Effective focal length	173.2 cm
Preferred detector type	CCD
Physical pixel size	21 x 21 microns
Angular pixel size	2.5 x 2.5 arc sec
Minimum Field of View (FOV)	44 x 44 arcmin
Minimum array size	1056 x 1056 pixels
FOV with selected array	53.3 x 53.3 arcmin

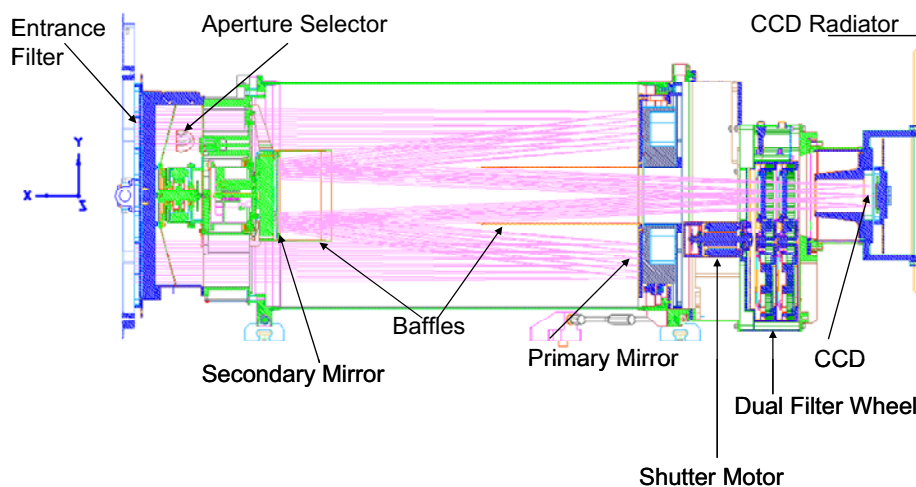* Defined here as the distance between the primary mirror vertex and the focal plane.

Figure 3. Cross section of the SUVI optical system showing optical rays and relative positioning of all the optical elements.

4. DETAILED SUVI IMAGE QUALITY PREDICTIONS

Surface scatter phenomena continues to be an important issue in diverse areas of science and engineering in the 21st century. In particular, image degradation due to surface scatter from residual optical fabrication errors remains a serious problem in many short wavelength (X-ray/EUV) imaging applications.

Most currently-available image analysis codes (ZEMAX®, Code V, ASAP, FRED, etc.) require the scatter behavior, i.e. the bi-directional reflectance distribution function (BRDF) data as input in order to calculate the image quality from such systems. This BRDF data is difficult to measure and rarely available for the operational wavelengths of interest. Since the smooth-surface approximation is often not satisfied at these short wavelengths, the classical Rayleigh-Rice[10,11] expression that indicates the BRDF is directly proportional to the surface power spectral density (PSD) cannot be used to calculate BRDFs from surface metrology data for even slightly rough ($\sigma > 0.02\lambda$) surfaces.

Image quality predictions as degraded by surface scatter effects thus involves a two-step process: (i) first, one must be able to predict the scattered light behavior, or BRDF, from measured (or assumed) surface metrology data, and (ii) then one must be able to calculate the image degradation from that scattered light behavior.
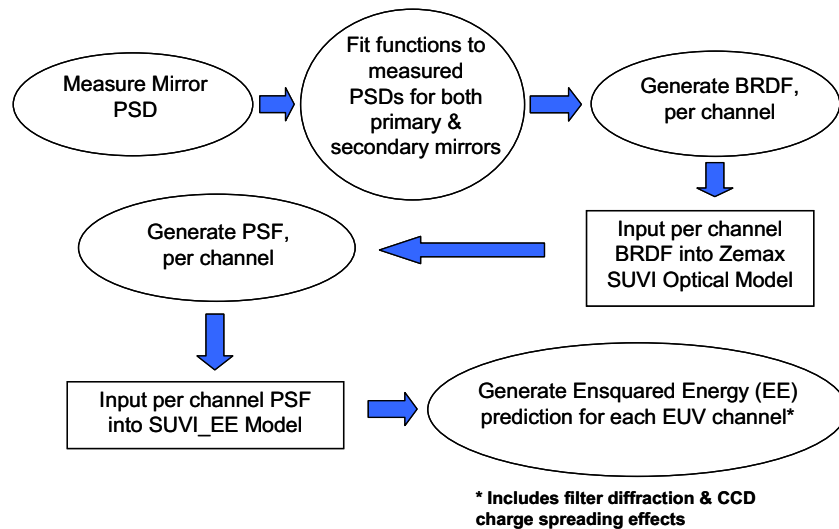

Figure 4. Forward modeling technique used to estimate the imaging performance or the fractional ensquared energy performance of SUVI.

4.1 Brief review of the GHS Scattering Model

Scattering effects from micro-topographic surface roughness are merely diffraction phenomena resulting from random phase variations in the reflected wavefront. Rayleigh-Rice (1951)[10] or Beckmann-Kirchhoff (1963)[12] theories are commonly used to predict surface scatter effects. Also, Harvey and Shack (1976)[13,14] developed a linear systems formulation of surface scatter phenomena in which the scattering behavior is characterized by a surface transfer function. This treatment provided insight and understanding not readily gleaned from the two previous theories. However, smooth surface and/or paraxial approximations have severely limited the range of applicability of each of the above theoretical treatments.

A new linear systems formulation of non-paraxial scalar diffraction theory[15-17] applied to surface scatter phenomena resulted first in an empirically modified Beckmann-Kirchhoff surface scatter model,[18,19] then a generalized Harvey-Shack (GHS) theory[20,21] that produces accurate results for rougher surfaces than the Rayleigh-Rice theory and for larger incident and scattered angles than the classical Beckmann-Kirchhoff theory. These new developments simplify the analysis and understanding of non-intuitive scattering behavior from rough surfaces illuminated at large incident angles.

At the heart of this linear systems formulation of surface scatter theory is the following expression for the surface transfer function that relates surface scatter behavior to surface characteristics,

$$H_s(\hat{x}, \hat{y}; \gamma_i, \gamma_s) = \exp\left\{-\left[2\pi\sigma_{rel}(\gamma_i + \gamma_s)\right]^2\left[1 - C_s(\hat{x}, \hat{y})/\sigma_{rel}^2\right]\right\}, \qquad (1)$$

where σ_{rel} is the band-limited *relevant* (or effective) rms surface roughness[22,23] obtained by integrating the surface power spectral density (PSD) over spatial frequencies from zero to $1/\lambda$, $\gamma_i = \cos\theta_i$, $\gamma_s = \cos\theta_s$, and $C_s(\hat{x}, \hat{y})$ is the autocovariance (ACV) function. The BRDF is then given by

$$BRDF = Q\,\mathsf{F}\left\{H(\hat{x}, \hat{y}; \gamma_i, \gamma_s)\right\} \qquad (2)$$

where the polarization reflectance factor Q has been substituted for the scalar reflectance R. The only other formula required is the following expression for the total integrated scatter (TIS)

$$TIS = 1 - \exp[-\left(4\pi\cos\theta_i\,\sigma_{rel}/\lambda\right)^2]. \qquad (3)$$

Unlike the original Harvey-Shack (OHS) surface scatter theory[13,14] with its paraxial assumption that allowed a single surface transfer function that resulted in the claim of shift-invariant BRDFs when expressed in terms of the direction cosines of the incident and scattered angles, Eq. 1 is the mathematical description of a two-parameter family of surface transfer functions, one for each angle of incidence (θ_i) and each scattering (θ_s) angle. This is what makes the GHS scatter theory so computationally-intensive. For each two-dimensional numerical Fourier transform calculated, we save only the single data point that satisfies the two parameters γ_i and γ_s. For surfaces with isotropic roughness, one needs only to perform the computations for a one dimensional radial profile of scattering angles; i.e., we can use a Hankel transform algorithm.

The BRDF calculation methodology is outlined as follows:[24]

- A fit is made to the measured (or assumed) surface PSD using sums of ABC (K-correlation) and/or Gaussian functions.

- The resulting analytical expression for the surface ACV function is calculated.

- The ACV function is then inserted into Eq. 1 and an FFTLog transform (2000 pts) is performed for each scattering angle of interest to obtain the BRDF profile.

- The BRDF is re-normalized so that its 2-D integral equals the TIS given by Eq. 3.

This new surface scatter model has been quazi-vectorized by merely substituting the polarization reflectance factor, Q, for the reflectance, R, in an otherwise scalar treatment. Predictions from the GHS surface scatter theory were originally validated for moderately rough surfaces at large incident angles for the special cases of a Gaussian PSD function[20,21] and for the non-paraxial behavior of sinusoidal phase gratings[25]. However, the use of a conventional FFT algorithm in calculating BRDFs with the GHS surface scatter theory proved to be too computationally-intensive to be practical for surfaces exhibiting inverse power law PSDs in which the relevant spatial frequencies often span a dynamic range of 6 to 8 decades.

The implementation of the FFTLog algorithm was a major advance that enabled us to perform numerical Hankel transforms over an incredible twenty-five (25) decades of dynamic range in spatial frequency for a function which is well-behaved in $\ln f$.[24] We outline below a few details of the FFTLog Hankel transform algorithm[26]:

- *FFTLog* is a set of subroutines that compute the fast Fourier or Hankel (i.e., Fourier-Bessel) transform of a periodic sequence of logarithmically spaced data points.

- *FFTLog* can be regarded as a natural analogue to the standard Fast Fourier Transform (FFT), in the sense that, just as the normal FFT gives the exact (to machine precision) Fourier transform of a linearly spaced periodic sequence of data points, so also *FFTLog* gives the exact Fourier or Hankel transform, of arbitrary order, of a logarithmically spaced periodic sequence of data points.

- *FFTLog* shares with the normal FFT the problems of ringing (response to sudden steps) and aliasing (periodic folding of frequencies), but under appropriate circumstances *FFTLog* may approximate the results of a continuous Fourier or Hankel transform.

- The *FFTLog* algorithm is particularly useful for applications where the power spectrum extends over many orders of magnitude in spatial frequency *f*, and varies smoothly in ln*f*.

The "ringing" and "aliasing" effects inherent to numerical Fourier transform calculations eventually limit the achievable dynamic range over which an accurate calculation can be made.[24]

An exhaustive review of the generalized Harvey-Shack (GHS) surface scatter theory, and its validation for both rough surfaces and non-paraxial incident and scattering angles, is given by Krywonos et al.[27] Furthermore, the excellent agreement (for specific test cases) with NASA's in-house optical surface analysis code (OSAC) which was developed for detailed image analysis of X-ray/EUV imaging systems (both normal and grazing incidence) adds to our growing level of confidence in this new numerical tool for modeling scattered light behavior for a broad range of applications involving moderately rough surfaces.

4.2 Characterizing the scattering surface

It often takes three, or even four different metrology instruments to measure the surface characteristics over the entire range of relevant spatial frequencies for a given application. Figure 5 illustrates the metrology data taken from (*i*) a full-aperture interferometer, (*ii*) a micro phase-measuring interferometer (μPMI) with a 2.5X objective, (*iii*) a μPMI with a 50X objective, and finally (*iv*) an atomic force microscope (AFM). These measurements were carried out at IOS-Tinsley where the SUVI mirrors are machined, figured and polished to their final specifications.
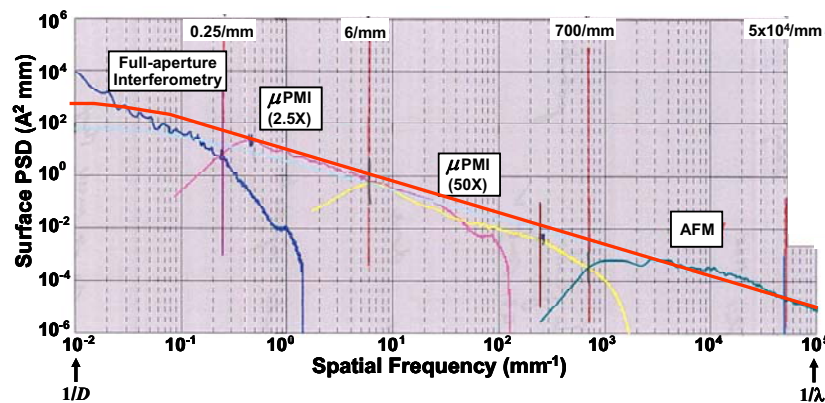

Figure 5. The composite surface power spectral density (PSD) function determined from four different metrology instruments. An ABC, or K-correlation, function has been fit to the experimental data to characterize the surface over the entire range of relevant spatial frequencies.

Each metrology instrument is inherently band-limited and the response falls off at spatial frequencies both above and below its range of applicability. However, when we superpose the output from the different instruments, we can fit an appropriate function to the composite surface PSD curve. Surface roughness spanning the spatial frequency range $1/D < f < 1/\lambda$, where D is the diameter of the illuminated portion of the optical element and λ is the operational wavelength, can degrade image quality. Since only a portion of the optic is illuminated at one time, we might have $D \sim$ 100 mm and $\lambda = 100$ Å. This yields seven (7) decades of dynamic range in spatial frequency over which we have to specify and measure the surface characteristics. An ABC, or K-correlation, function of the form

$$PSD(f_x)_{1-D} = \frac{A}{[1+(B f_x)^2]^{C/2}} ,$$

(4)

has been fit to the experimental data in Figure 5. Assuming isotropic roughness, this one-dimensional (1-D) measured surface PSD can be converted to the following 2-D surface PSD that relates more directly to the surface scatter behavior, and hence to the resulting image degradation,

$$PSD(f)_{2-D} = K \frac{A\,B}{\left[1+\left(B\,f\right)^2\right]^{(C+1)/2}} \quad, \quad K = \frac{1}{2\sqrt{\pi}} \frac{\Gamma\left((C+1)/2\right)}{\Gamma\left(C/2\right)}. \tag{5}$$

For $C > 1.0$, there is also a convenient analytical expression for the volume under the two-dimensional surface PSD,

$$\sigma^2_{Total} = \frac{2\pi\,KAB}{\left[(C-1)B^2\right]}, \text{ for } C > 1.0. \tag{6}$$

The integral under the 2-D surface PSD does not converge for $C \leq 1.0$. There is even an analytical expression for the two-dimensional Fourier transform of the above two-dimensional surface PSD. This surface autocovarance function is given by

$$ACV(r) = (2\pi)^{1/2} \frac{A}{B} \frac{2^{-C/2}}{\Gamma(C/2)} \left(\frac{2\pi\,r}{B}\right)^{(C-1)/2} K_{(C-1)/2}\left(\frac{2\pi\,r}{B}\right). \tag{7}$$

In the above expressions A, B, and C are fitting parameters. From the grating equation we obtain

$$f_x = \frac{\sin\theta_s\,\cos\phi_s - \sin\theta_i}{\lambda}, \quad f_y = \frac{\sin\theta_s\,\sin\phi_s}{\lambda}, \tag{8}$$

Also, $f = \sqrt{f_x^2 + f_y^2}$, $r = \sqrt{x^2 + y^2}$, and $K_{(c-1)/2}$ is the modified Bessel function of the second kind.
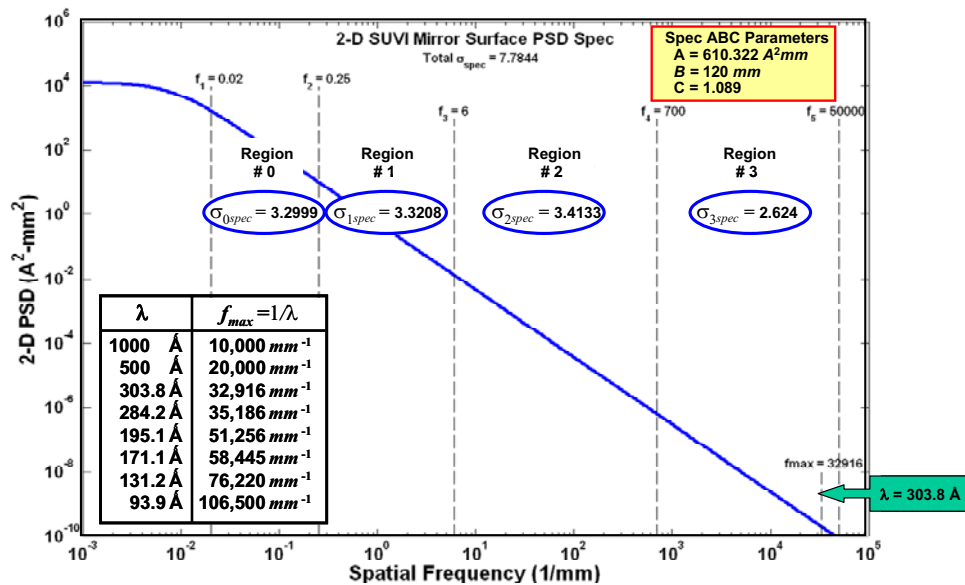

Figure 6. SUVI mirror specification and the maximum relevant spatial frequency.

4.3 Estimating the BRDFs resulting from the SUVI "spec" PSD

Using the metrology data from Figure 5 (taken for one of the mirrors of the *state-of-the-art* atmospheric imaging assembly, AIA[28], which is on board the solar dynamics observatory, SDO) a single ABC function was fit as an aid to

establishing the SUVI mirror specification PSD (*aka* "spec" PSD) shown in Figure 6. We wish to emphasize that there is a wavelength-dependent maximum spatial frequency, f_{max}, beyond which the roughness does not degrade the image quality due to scatter. The ABC parameters are indicated on the figure as are the maximum relevant spatial frequencies for each of the wavelengths that we are modeling. Note that the band-limited rms roughness (in Å) is also marked on the graph for each of the metrology regions.

Figure 7 shows the corresponding cumulative surface roughness obtained by integrating the surface PSD. The value of the "relevant" roughness is indicated on the graph for a wavelength of 303.8 Å. The relevant roughness and TIS, as calculated from Eq. 3, are tabulated for all wavelengths to be modeled.

The Fourier transform of the surface ACV function was then calculated both analytically and numerically, and compared. The "ringing" and "aliasing" effects inherent to numerical Fourier transform calculations are visible in Figure 8; however, for these values of the ABC parameters, the FFTLog algorithm is accurate over 25 decades of variation in spatial frequency.
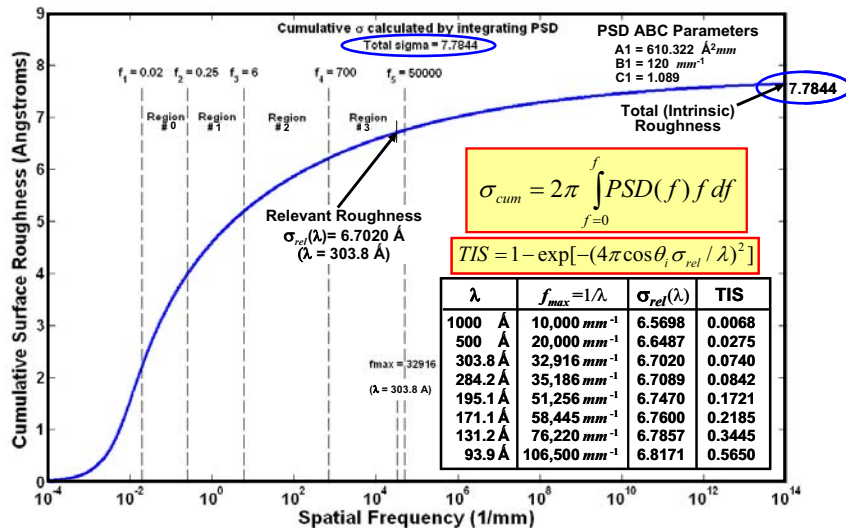

Figure 7. Cumulative surface roughness for SUVI spec PSD.
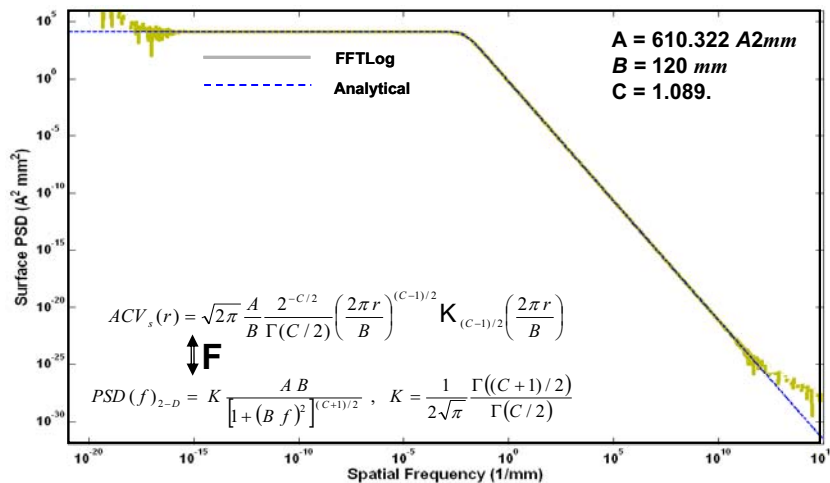

Figure 8. Validation of the FFTLog Hankel transform algorithm over a dynamic range of twenty-five (25) decades for the ABC Function that describes the PSD in Figure 6.

Figure 9 shows the BRDF profiles as predicted by the GHS surface scatter theory with the FFTLog algorithm for the PSD shown in Figure 6 for the six SUVI wavelengths plus two longer wavelengths for which the PSD approached a

"smooth" surface. Note that the total integrated scatter (TIS) as calculated by Eq. (3) varies from less than 1% for λ = 1000 Å to over 56% for λ = 93.9 Å. The BRDF profiles also appear to have a similar shape as the surface PSD; however, the scattered radiance increases and the shoulder shifts to the left with decreasing wavelength. The slope of the inverse power law function does not appear to change significantly with wavelength. Having calculated these BRDFs we can interpolate and sample at specific angles to use as input into ZEMAX® to calculate the telescope point spread functions and fractional ensquared energy data.
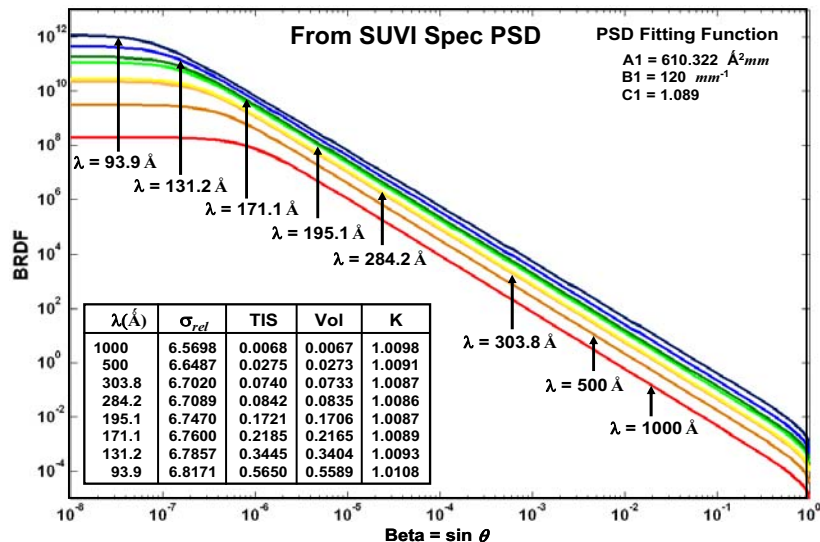

Figure 9. BRDF profiles for representative SUVI mirror PSD.

4.4 BRDF Predictions for the "as manufactured" SUVI Mirrors

Predicting the "as-manufactured" performance of the SUVI telescopes will follow the procedure described in the previous section. As each SUVI mirror is figured and polished to achieve at a minimum, the surface microroughness performance called out in Figure 6, measurements taken of the surface demonstrate that the "spec" PSD shown is achievable.
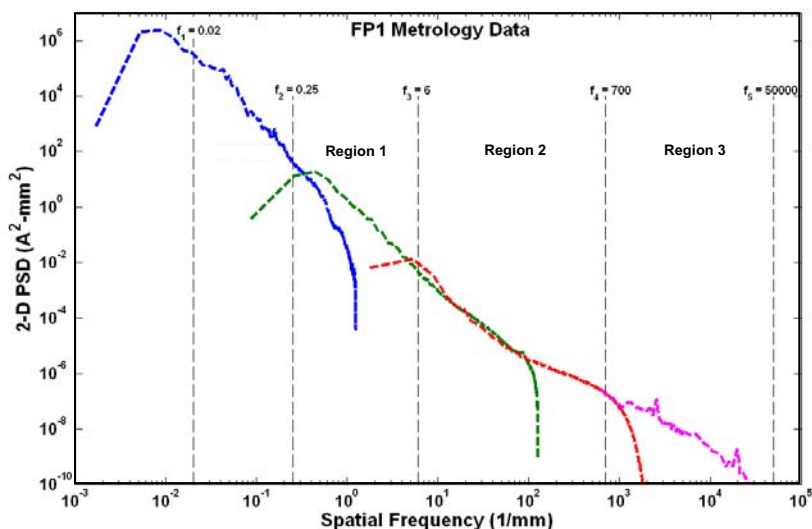

Figure 10. Metrology data from the first SUVI primary mirror (FP1).

Figure 10 shows the metrology data from the first manufactured SUVI flight primary mirror (FP1). These measurements were taken of the uncoated surface of the optic. Metrology data was obtained from three different instruments as

described above in §4.2, using a full aperture interferometer, an optical profilometer and an AFM. One can see the inherent band-width limits of the various instruments where the component PSDs fall off at the ends of their respective spatial frequency ranges. Similar measurements were taken for the secondary mirror, FS1. Note that by superposing the overlapping band-limited PSDs obtained from the various metrology instruments we can fit a smooth curve to the measurement data to describe the surface PSD over the entire range of relevant spatial frequencies. Figure 11 shows a smooth fit to the measured metrology data shown in Figure 10, using a Gaussian and two ABC functions (green curves on the graph). The black curve is the sum of those three fitting functions and provides an excellent fit to the metrology data. The defining parameters of the three fitting functions are provided in the upper right of the figure. The lack of a good fit to the measured curve at the extreme low spatial frequencies are of no concern as there are separate surface figure and slope error specifications at this spatial frequency regime that drive the performance and tolerance on the core point spread function of the instrument. Similarly, for the FS1 PSD metrology data, we fit a sum of three ABC functions shown in Figure 12.
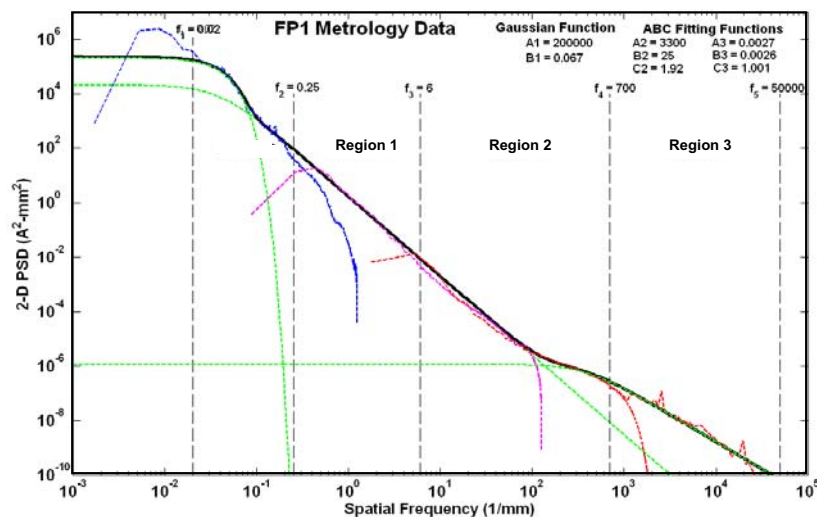

Figure 11. Illustration technique for fitting a smooth function to metrology data of the first SUVI primary mirror, FP1.
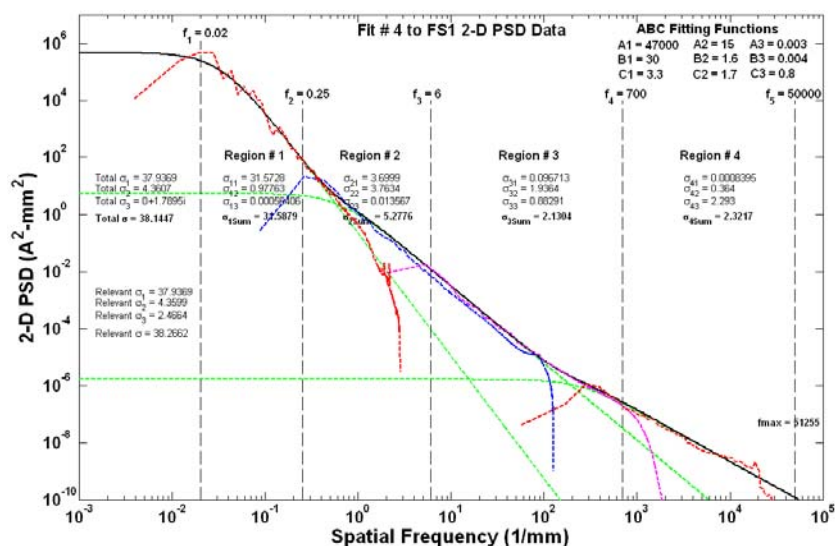

Figure 12. Smooth function fit to the metrology data from the first SUVI secondary mirror, FS1.

4.5 BRDF profiles predicted for SUVI mirrors FP1 & FS1

Because we are able to fit the measured PSD curves for both FP1 and FS1 mirrors using sums of ABC functions and Gaussians, we can use the same BRDF estimation technique discussed in §4.2 and §4.3. Via this approach we calculated the BRDFs for both mirrors and the results are illustrated in Figures 13 and 14. Since both curves are re-normalized such that the TIS is equal to that predicted by the σ_{rel} for the respective surface PSD, the BRDFs are identical for angles greater than that corresponding to the half-width of a detector pixel (= 2.5 x 2.5 arc sec^2). In other words, the additional scattered light produced by the BRDF is scattered at small angles that it will not result in any significant image degradation. These BRDF curves are also interpolated and sampled (but in a log-linear data format) at the specific scattered angles desired for insertion into ZEMAX® for calculating the PSF profiles and the fractional ensquared energy values to estimate SUVI EUV performance.

Figure 13 illustrates the calculated BRDF profiles calculated from the PSD fit to the metrology data for FP1 for all six SUVI wavelengths and two longer wavelengths of 500 and 1000 Å. Note the highlighted region where some non-intuitive crossing over of profiles occurs (although this occurs at very small scattering angles that in practice will not be discernable from the specular beam). Figure 14 is similarly annotated with respect to wavelength coverage for FS1.
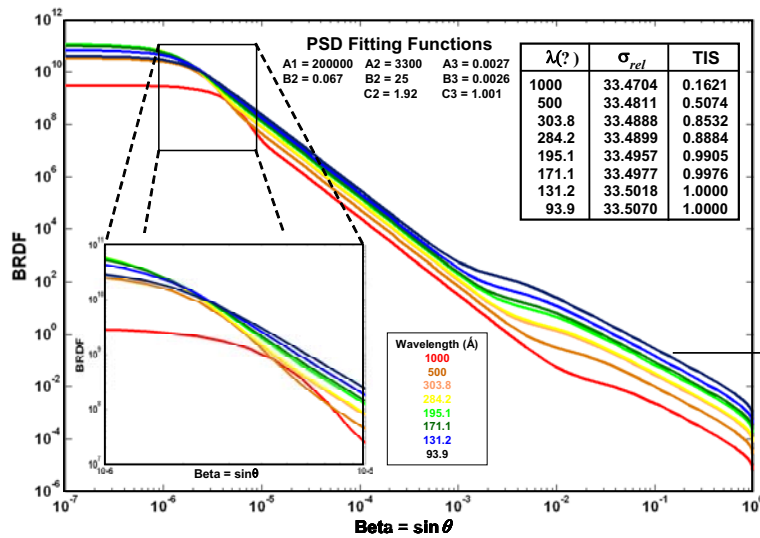

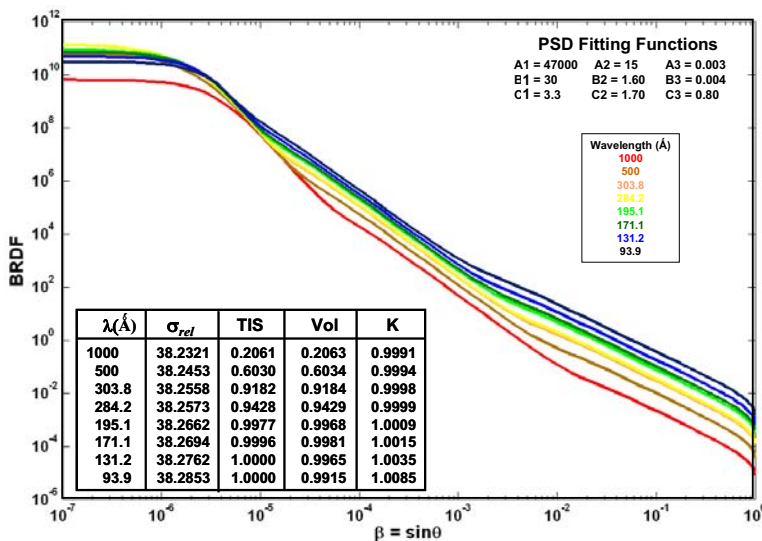Figure 13. BRDF prediction of the FP1 PSD metrology data.

Figure 14. BRDF prediction of the FS1 PSD metrology data.

4.5.1 Peterson's in-field stray light treatment

Before going on to the next section, we comment briefly on another effort we carried out that involved the generalization of a simple and elegant analytical treatment of in-field stray light in multi-element imaging systems reported by Peterson in 2004.[29]

Peterson's treatment was based upon both a smooth-surface and a paraxial assumption. However, under those conditions he derived (by the application of the Lagrange invariant from 1st-order image formation theory and the application of the conservation of radiance; i.e., the brightness theorem) a simple expression for the irradiance distribution in the focal plane of a multi-element imaging system as degraded by in-field stray light. Given the BRDFs of the optical surfaces involved, the resulting analytical formula allows quick and easy parametric image quality predictions without the brute-force, cumbersome and computationally-intensive calculations required by ZEMAX® and ASAP for performing accurate image analysis involving scattered light.

EUV telescopes satisfy the paraxial assumption in Peterson's treatment; however, the smooth-surface assumption is frequently not satisfied for very short EUV wavelengths, even for state-of-the-art optical surfaces.

We have therefore generalized the Peterson analytical treatment (for two-mirror telescopes such as SUVI) by adding a term for the scattered-scattered radiation in the expression for the irradiance in the telescope focal plane. This generalized expression has been validated by both ZEMAX® and ASAP calculations for a two-mirror EUV telescope with 1st-order design parameters similar to the SUVI telescope design. The results of this work are described by Harvey et al.[30]

4.6 Determining the in-band PSF from the BRDFs

There are two parts to our approach to predicting the point spread function (PSF) for SUVI. We first use the ZEMAX® ray trace program in the non-sequential mode to compute the encircled energy at the focal surface as a function of field angle. Scattering is explicitly included using the BRDF calculations described above in §4.2 and §4.3. We then decompose the encircled energy function by considering it as a series of narrow, concentric rings centered on the geometric core of the image. Using a method of successive differences, we compute the mean irradiance in each ring. The set of mean values, stated as a function of field angle, is the required PSF. We adopted this approach in lieu of using the PSF capabilities of ZEMAX® because of computational difficulties with the latter.
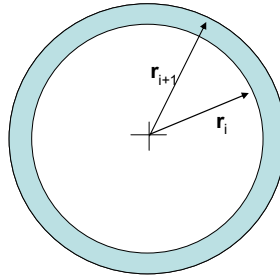

Figure 15. Geometry for PSF calculations made at the detector focal plane.

Thus, we consider an array of concentric circular rings, centered on the geometric image and let the ith ring be defined as the shaded area between radii r_i and r_{i+1}, as shown in Figure 15. The area of the ith ring, A_i will be given by

$$A_i = \pi(r_{i+1}^2 - r_i^2) \tag{9}$$

The mean irradiance in the ith ring will be

$$I_i(r_i) = \frac{E_i}{A_i} = \frac{E_i}{\pi(r_{i+1}^2 - r_i^2)} \equiv PSF_{tel}(r_i) \tag{10}$$

where E_i is the increment of encircled energy associated with the ith ring. The set of mean irradiance values, $I_i(r_i)$, together with the corresponding radii, r_i, approximates the required PSF. The approximation can be as accurate as desired by making the rings sufficiently narrow. In the limit 0 $(r_{i+1} - r_i) \rightarrow 0$, the approximation becomes exact. Note that the rings do not all need to have the same width; they can be very narrow in regions where the PSF is changing rapidly (i.e. in the vicinity of the geometric image) and can be wider where it is changing gradually.

The calculation of the E_i values at each r_i are done with the ray trace program, ZEMAX®, as discussed in the next section. Once the table of encircled energy values has been compiled, the calculation of the corresponding PSF values is easily carried out, using the above expression for $I_i(r_i)$.

4.6.1 ZEMAX®

The application of ZEMAX®[¥] to the SUVI scattering problem requires the following steps:

(a) preparation of a suitable geometric model of the optical system,
(b) use of the non-sequential mode,
(c) selection of an appropriate set of scattering angles,
(d) computation of the BRDF value at each scattering angle,
(e) formatting the BRDF values for insertion into ZEMAX®,
(f) selection of an appropriate set of radial position ranges for the encircled energy calculation,
(g) computation of the encircled energy function and compiling the results.

The Geometric Model: The geometric model for the SUVI optical system was first established using the sequential mode of ZEMAX®. This model was developed through a number of iterations as the mechanical design, the CCD array size and the pointing strategy evolved. The SUVI ZEMAX® model contains all baffles and apertures as well as Zernike coefficients for the optics and was used to verify the geometrical performance of the optical system. A slightly simplified model of the system was implemented in the non-sequential mode of ZEMAX® to facilitate the scattering calculations. The Zernike terms and some of the apertures were omitted in the interest of simplicity. This non-sequential model has been used for all scattering calculations and includes a set of alignment errors that have been introduced to evaluate an extreme worst-case for the geometric performance. Every term was set to its maximum allowed value and the sign of each term was adjusted so as to maximize the size of the on-axis geometric core of the image. Thus, these assumptions define a worst-case for the optical internal alignment errors. The assumed values of the error terms are given in Table 2.

Table 2. Error terms assumed for the geometrical model used in the scattering predictions

Assumed Alignment Errors

Element	X Error (cm)	Y Error (cm)	Tilt about X (arcmin)	Tilt about Y (arcmin)
Primary Mirror	0.02	-0.02	-0.02	-0.02
Secondary Mirror	-0.02	0.02	0.067	0.067

The ZEMAX® Non-Sequential Mode: The scattering properties of each mirror were introduced by including a table of BRDF values (taken from the data shown in Figures 13 and 14) as part of the assumed coating definition for each mirror. This table is read into the program by means of a table-reading extension that is supplied with ZEMAX®. We specified a value of 100 for the number of rays to be considered in the scattering calculation (the maximum allowed by the code).

Scattering Angle Selection: The scattering angles are carefully chosen since ZEMAX® does not interpolate between tabulated BRDF values and the dynamic range of the scattering function required for the SUVI optics is many decades. We solved the dynamic range problem by defining the BRDF for scattering angles that are equally spaced in the logarithm of the scattering angle. The range of scattering angles must extend from values small compared to a CCD pixel to something larger than the subtended angle of the CCD. We chose an angular range extending from $\theta = 10^{-6}$ degrees to

---

[¥] http://www.zemax.com/

$\theta = 10$ degrees and defined ten angles for each decade (*log $\Delta\theta$ = 0.1*). These choices were found to produce excellent results.

Radial Position Ranges: By trial and error we found that the sequence 10μ, 20μ, 50μ, 100μ, 200μ, 500μ... etc., for the maximum radial distance parameter gave the best results for calculating the encircled energy (per Eq. 10).

PSF Calculations: Computation and compilation of the encircled energy function begins with the smallest radial range of 10 microns. When the computation is complete, the PSF calculations according to Eq. 10 can be carried out. Radial steps of 1 micron were used between the distance range from 0.0 to 10.0 microns, and subsequently repeated for larger radial ranges 20μ, 50μ, 100μ, etc. but increasing the step size appropriately to stay within the computational capability of ZEMAX®. When complete, we convert the radial distances to angular distance, arc seconds; smoothing out all discontinuities to achieve the results shown in Figure 16.

Figure 17 shows ZEMAX® modeled SUVI images of a point source for the shortest (93.9 Å) and longest (303.8 Å) EUV channels using inputted BRDFs produced for both the "spec" PSD case [which is assumed for both mirrors in panels (a) and (c)] and the PSD measurements for FP1 and FS1 [panels (b) and (d)]. The size of the reference box shown is 5 x 5 arc sec^2 (equal to 2 x 2 SUVI pixels). One can see that the shortest EUV wavelength shows a more substantial amount of small-angle scattering compared to the longer wavelength. Nevertheless, the boundaries of the geometric image for each case are well-defined in the minimum 2 x 2 pixel resolution element.
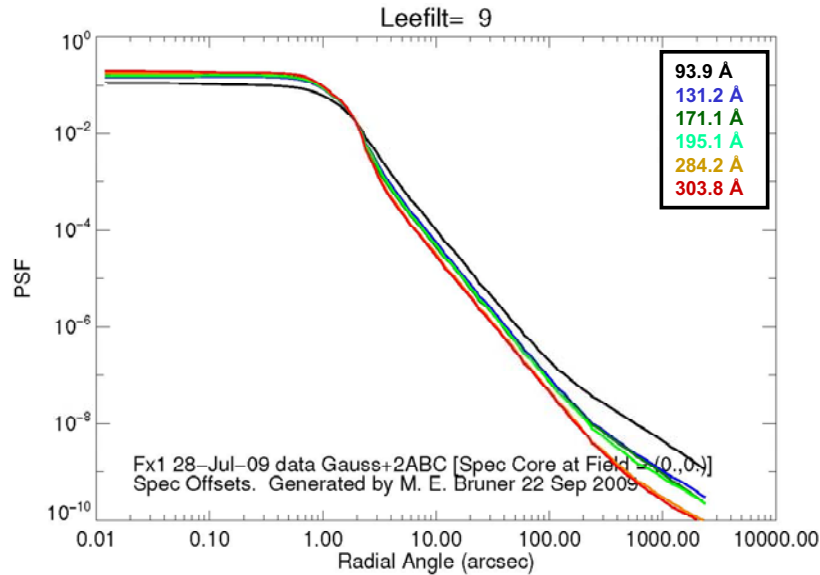

Figure 16. PSFs calculated using the SUVI ZEMAX® model with BRDF inputs based on measured PSDs for FP1 and FS1. PSFs shown have been smoothed using a Lee filter with box = 9.

4.7 Predicting the ensquared energy

The last step of the forward model calculation involves estimating the fractional ensquared energy (EE) performance for SUVI. This is determined via convolution of the in-band PSFs shown in Figure 16 with the PSF (or "smoothing") functions corresponding to each of the other optical elements of the instrument. Namely, the entrance and focal plane filters which further diffract EUV photons and the CCD which spreads the electron charge generated by an absorbed photon.

The fractional ensquared energy (EE, which is a unitless fraction between 0 and 1), $EE(n,\lambda_i)$, is defined as the ratio of integrals of the total telescope point-spread function, $PSF_{tel}(x,y,\lambda_i)$, integrated over an n x n ensquared (or enpixeled) instantaneous-field-of-view on the CCD (of area = x_n x y_n subtending n x n arcsec^2), divided by the $PSF_{tel}(x,y,\lambda_i)$ integrated over the total FOV subtended by the CCD. $PSF_{tel}(x,y,\lambda_i)$ is in turn calculated as a set of convolutions [denoted by "$f * g$" in Eq. (12)] of the in-band, normalized point spread functions of the filters, mirrors and the CCD. Thus, $EE(n,\lambda_i)$ is:

$$EE\left(n,\lambda_i\right) = \int\limits_{x_n,y_n} PSF_{tel}(x,y,\lambda_i)dxdy \left/ \int\limits_{CCD} PSF_{tel}(x,y,\lambda_i)dxdy \right. ,\qquad(11)$$

where

$$PSF_{tel}(x,y,\lambda_i)dxdy \equiv PSF_{ent}(x,y,\lambda_i) \;*\; PSF_{mir}(x,y,\lambda_i) * PSF_{fp,j}(x,y,\lambda_i) * PSF_{CCD}(x,y,\lambda_i)\qquad(12)$$

Here, $PSF_{ent}(x,y,\lambda_i)$ is the point spread function due to diffraction of the entrance filter; $PSF_{fp,j}(x,y,\lambda_i)$ is the point spread function due to the focal plane filter, j (= 1,2 for two filter wheels); $PSF_{mir}(x,y,\lambda_i)$ is the point spread function due to the mirrors (which includes the geometric core function and EUV scattering effects); and $PSF_{CCD}(x,y,\lambda_i)$ is the point spread function due to CCD charge spreading effects. The filters (manufactured by Luxel Corporation) diffract the EUV photons due to the Ni mesh upon which the thin metallic films (~ 2000 Å) are deposited, this mesh has a line density of ~ 70 lines/in yielding a total transmittance of ~ 82%. Finally, we note that there's *no loss of generality* to normalize the EE over the CCD because integrating further out to 2π sr gains only a very small fraction of a percent in the calculation. For SUVI, the results of the EE calculation are shown in Figure 18.
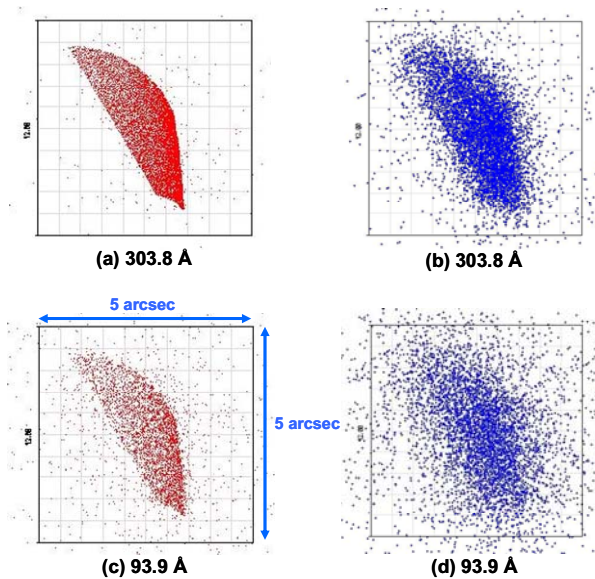

Figure 17. PSF images determined using SUVI ZEMAX® model with BRDF inputs for shortest and longest EUV channels. Panels (a) and (c) show the response (in 5 x 5 arc sec^2 boxes) due to the BRDF constructed from the PSD shown in Figure 6. Here we found that the TIS is moderate: 7.4% at 303.8 Å and 56% at 93.9 Å and spots are well-defined (note that SUVI has a wavelength aperture selector that is a "pie" shape to allow selection of any one of the six EUV channels, hence the oblong shape of the PSF). Panels (b) and (d) show the forward modeled response for the SUVI flight mirror pairs, FP1 and FS1, and here we see that the TIS is strong: 85% to 90% at 303.8 Å and 100% at 93.9 Å. Geometric spots are not as well defined but the energy still concentrates in the minimum resolution box size of 2 x 2 pixels.
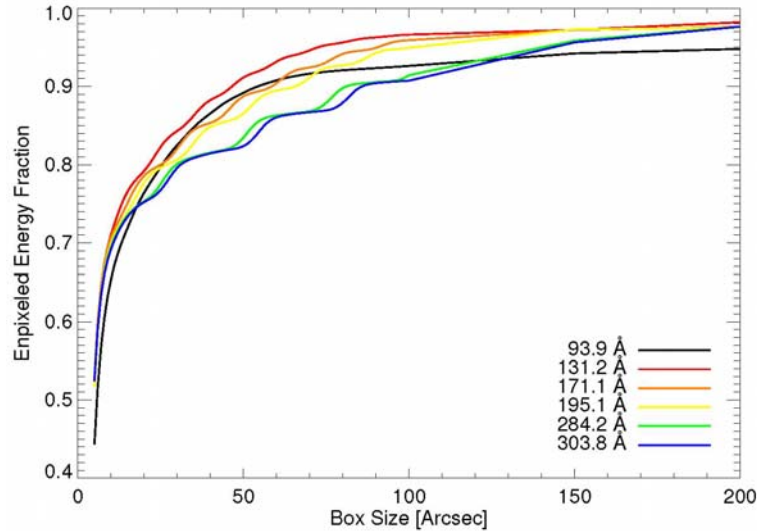
Figure 18. Ensquared energy calculation for SUVI based on measured PSDs of the uncoated flight mirrors, FP1 and FS1. The structure in the plots is caused by the filters' diffraction pattern which is being integrated as one goes to larger and large *n* x *n* pixel box sizes.

4.8 Effects of multilayer coatings on ensquared energy predictions

The multilayer coatings on the telescope mirrors can influence EUV light scattering in two ways: 1) the coating can alter the roughness of the mirror and 2) interference effects can occur from the light scattered from the different interfaces within the multilayer. The influence of multilayer coatings on mirror roughness via a linear growth model has been developed at LBNL (along with other collaborators) and compared to previous experimental results using Mo/Si coated optics deposited at LLNL, using DC magnetron sputtering.[31, 32] In the LBNL model, the added interference effects due to the multilayers are calculated using the distorted wave Born approximation (DWBA) which has been validated with measurements of the BRDF of the Mo/Si multilayer coatings.

4.8.1 Multilayer scattering effects

Measurements of the scattered EUV light were made of the Mo/Y 93.9 Å segment of the coated FP2 mirror (i.e., "flight primary mirror #2", which is fabricated to the same design specifications as FP1) and compared with the predictions using the forward model described herein.[‡] These measurements were performed at the Lawrence Berkeley National Laboratory - Advanced Light Source (LBNL-ALS), beamline 6.3.2. The measurements were taken with a fixed incident angle of 5 degrees by scanning the detector angle. The Bragg wavelength is shifted slightly shorter from the design wavelength of 93.9 Å due to the 5 degree incident angle. The measurements were performed using a channeltron with an acceptance angle of +/- 0.12 deg, about 1/10 the angular acceptance of the photodiode used for the reflectivity measurements. We can see in Figure 19 that the measured BRDF for FP2 drops off at angles above about 1.5 degrees in qualitative agreement with the calculated BRDF using the forward model described herein. Note that the latter does not include modeling of the multilayers. Although there is reasonably good agreement, the forward modeled BRDF is more conservative in its predictions, particularly at large angles. The uncertainty in the measured BRDF is better to within ± 10%.

The result of the ALS measurements found that the multilayer coating mainly affects scattering at angles outside the SUVI CCD field of view and hence adds no further loss in image quality beyond that generated by the surface quality of the optic. The small loss in throughput which results from large angle scattering is mostly accounted for in the measured reflectivity of the flight coated mirrors. Hence, a correction was estimated for the light scattered outside the SUVI CCD field of view but within the acceptance angle of the detector used for the reflectance measurements.

[‡] Due to program schedule constraints, FP1 could not be measured at the ALS to characterize EUV scattering and thus, we instead measured FP2 to which we also applied the forward model analysis. Figure 19 shows the comparative results.
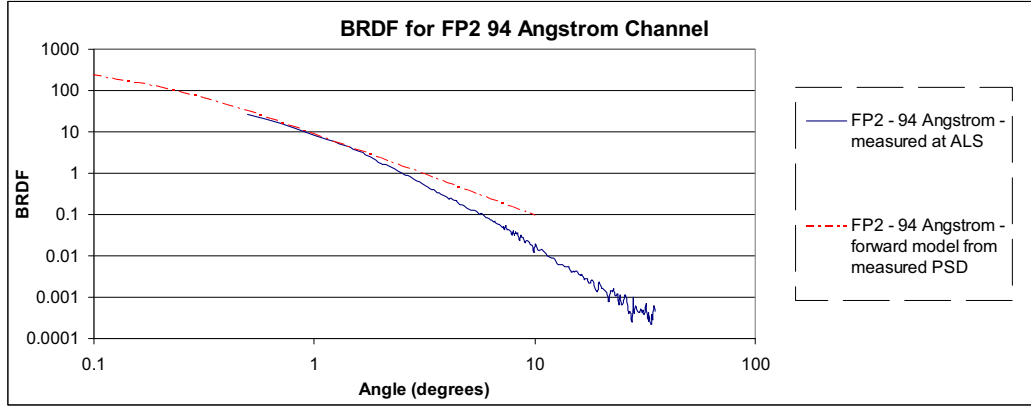
Figure 19. Comparison of measured BRDF for Mo/Y 93.9 Å coating on FP2 with forward modeled results for the uncoated FP2 mirror (which is identically fabricated to FP1). One can see that the predicted modeled results are slightly conservative in estimating the BRDF in comparison with measured FP2 results.

4.8.2 Reflectivity loss due to scattering

The scattered light that falls outside the SUVI CCD FOV is lost to the telescope and hence, is a loss in throughput. The acceptance of the detector used to measure the reflectivity at the ALS is slightly larger (+/-1.2 deg) than the FOV (+/-0.45 deg) of the SUVI detector, therefore some of this lost light will be included in the measured reflectivity. An upper limit to the correction needed to be applied to the measured reflectance can be obtained by integrating the BRDF for each of the mirrors. The integral of the BRDF for each of the wavelengths using the BRDF calculated with multilayer effects is given in Table 3. The table shows the relative scattering obtained by integrating the BRDF over a ring with an inner diameter determined by the CCD angular size and an outer diameter = 2.4 degrees. The multilayers have almost no effect on the correction. The correction is negligible for the secondary mirror since scattering angle to the SUVI CCD FOV is 2.54 times larger than for the primary mirror.

Table 3. The fraction of light scattered outside the SUVI FOV but within the ALS reflectance detector.

Wavelength	Primary (ML)	Secondary (ML)
(nm)	(%)	(%)
30.4	0.34	0.02
28.4	0.39	0.02
19.5	0.81	0.04
17.1	1.03	0.05
13.1	1.71	0.09
9.4	3.24	0.16

These corrections are applied to the throughput calculation of the SUVI telescope, given by the *effective area*, $A_{eff}(\lambda_i)$, for EUV channel centered at wavelength, λ_i, given by:

$$A_{eff}(\lambda_i) \equiv A_{eff}(\lambda_i, t, \mathbf{x})$$
$$= A_{\lambda_i} G f_{lin} q(\lambda_i) \rho_p(\lambda_i) \rho_s(\lambda_i) t_{ent}(\lambda_i) t_{fp,j}(\lambda_i) \eta(\mathbf{x}) ff(\mathbf{x}) c(\lambda_i, t) \qquad [\text{cm}^2]. \qquad (13)$$

Here A_{λ_i} is the geometric collecting area; G is the detector amplifier gain; f_{lin} is the linear response of the CCD; $\rho_p(\lambda_i)$ is the reflectivity of the primary mirror; $\rho_s(\lambda_i)$ is the reflectivity of the secondary mirror; $t_{ent}(\lambda_i)$ is the transmittivity[§] of the

---

[§] We use *transmittivity*, instead of *transmittance*, because the latter is equal to the integral of the transmittivity over a well defined waveband. The same holds for use of *reflectivity* versus *reflectance*.

entrance filter; $t_{fp,j}(\lambda_i)$ is the transmittivity of focal plane filter, j; $q(\lambda_i)$ is the quantum efficiency of the detector; $\eta(\mathbf{x})$ is the vignetting function at location $\mathbf{x}$ on the CCD focal plane; likewise, $ff(\mathbf{x})$ is the CCD flatfield function at location $\mathbf{x}$; and $c(\lambda_i,t)$ is the contamination loss function (of the entire instrument), measured over time, t. Each of the factors in Eq. (13) are either measured or modeled in order to calculate the effective area of the instrument.

Finally, using Equations 11-13, for each SUVI channel centered at EUV wavelength λ_i, we can calculate the *total system responsivity*, $S(n,\lambda_i)$, over an area of n x n arcsec^2 subtended on the focal plane:

$$S(n, \lambda_i) = EE(m, n, \lambda_i) A_{eff}(\lambda_i) \int_{(m\,x\,n\,\text{FOV})} I(\lambda_i, \Omega)d\Omega \qquad \text{[photons sec}^{-1}\text{ Å}^{-1}\text{]}. \quad (14)$$

Here, the fractional ensquared energy, $EE(n,\lambda_i)$, and the effective area, $A_{eff}(\lambda_i)$ are system metrics of performance, and $I(\lambda_i,\Omega)$ [photons cm^{-2} sec^{-1} sr^{-1} Å^{-1}] is the solar spectral radiance entering the telescope aperture that varies as a function of position observed over the solar disk (i.e., sr^{-1}). With appropriate modifications made to Eqs. 11-13 to account for the details of a specific EUV optical design, Eq. 14 can be applied to any EUV imaging system.

5. SUMMARY AND CONCLUSIONS

We have presented a novel forward model to estimate the EUV, in-band performance of the *solar ultraviolet imager* (SUVI). This model uses the measured PSDs of the first figured and polished mirror pair (FP1 and FS1) that were fabricated for the engineering development unit of SUVI. These mirrors were fabricated to the same design and performance specifications as all subsequent flight mirror pairs. The modeling technique involved estimating the in-band BRDF from each of the mirrors' measured PSDs and then inputting the BRDFs into the SUVI ZEMAX® model to produce in-band estimates of the PSFs for the combined mirrors. We then convolved each of the in-band PSFs with the PSFs produced by the entrance and focal plane filters (which incorporate diffraction effects due to the nickel mesh upon which the thin metallic films are deposited) as well as charge spreading effects due to the back-illuminated CCD, thus producing a measure of the total system PSF. The system PSF was then integrated over an m x n pixel array at the CCD focal plane and normalized by the same integral taken over the entire CCD array's field-of-view to calculate the fractional ensquared energy of the instrument for various n x n pixel arrays.

Further, the effects of the multilayer coatings on the scattering from the SUVI optics were investigated and reported. The BRDF was measured for the FP2 mirror's 93.9 Å coating and the measurements are in reasonably good agreement with the predicted results of the forward model described herein for the same, uncoated flight optic. Given the excellent quality of the super polished mirrors (per the measured PSDs), it is concluded that the multilayer coatings do not further affect the EUV scattering within the SUVI field of view and therefore do not degrade the fractional ensquared energy; however, the scattered EUV light that falls outside the SUVI CCD FOV leads to a small reduction in throughput. This loss is largely accounted for in the EUV measured reflectivity that is carried out for each multilayer coated optic (performed at the ALS beamline 6.3.2 at LBNL). From these measurements, there is a correction factor that is applied to the measured reflectivity of the mirrors to determine final system throughput, given by the effective area, $A_{eff}(\lambda_i)$. An estimated upper limit to this correction has been reported in Table 3.

Lastly, having calculated both the fractional ensquared energy and the effective area, the total system responsivitiy of SUVI is then calculated for an assumed (or measured) solar radiance, per EUV channel centered at wavelength, λ_i. Therefore, the forward model technique presented herein, can be utilized in a likewise fashion for predicting the in-band performance of any EUV imaging instrument.

6. ACKNOWLEDGEMENTS

7. REFERENCES

[1] For more information regarding the NOAA GOES satellites, see http://www.oso.noaa.gov/goes.

[2] J.-P. Delaboudiniere, R. A. Stern, A. Maucherat, F. Portier-Fozzani, W. M. Neupert, J. B. Gurman, R. C. Catura, J. R. Lemen, L. Shing, G. E. Artzner, J. Brunaud, A. H. Gabriel, D. J. Michels, J. D. Moses, B. Au, K. P. Dere, R. A. Howard, R. Kreplin, J. M. Defise, C. Jamar, P. Rochus, J. P. Chauvineau, J. P. Marioge, F. Clette, P. Cugnon and E. L. Van Dessel, "Imaging the solar corona in the EUV", Proc. COSPAR, ESA, 20, 2231-2237, 0273-1177, Birmingham, UK (1996).

[3] J. H. Underwood, M. E. Bruner, B. M. Haisch, W. A. Brown and L. W. Acton, " X-ray photographs of a solar active region with a multilayer telescope at normal incidence ", Science, New Series, 238, 61-64No. 4823 (1987).

[4] A. B. C. Walker, Jr., T. W. Barbee, Jr., R. B. Hoover and J. F. Lindblom, "Soft X-ray Images of the Solar Corona with a Normal-Incidence Cassegrain Multilayer Telescope", Science 241, 1781-1787 (1988).

[5] L. Golub and M. Herant, "Analysis of the 23 June 1988 flare using NIXT multilayer x-ray images", Proc. SPIE 1160, 629-635, San Diego, CA (1989).

[6] L. Golub, M. Herant, K. Kalata, I. Lavas, G. Nystrom, F. Pardo, E. Spiller and J. Wilczynski, "Sub-arcsecond observations of the solar X-ray corona", Nature 344 (6269), 842-844 (1990).

[7] A. B. C. Walker, Jr., J. F. Lindblom, R. H. O'Neal, M. J. Allen, T. W. Barbee, Jr. and R. B. Hoover, "Multi-Spectral Solar Telescope Array", Optical Engineering 29 (6), 581-591 (1990).

[8] A. B. C. Walker, II, M. J. Allen, C. E. DeForest, C. C. Kankelborg, D. S. Martínez-Galarce, J. E. Plummer, R. B. Hoover, T. W. Barbee, Jr. and D. B. Gore, "The Multi Spectral Solar Telescope Array VIII: The Second Flight", Proc. SPIE, 2515, 182-193, San Diego, CA (1995).

[9] D. S. Martínez-Galarce, A. B. Walker, D. B. Gore, C. C. Kankelborg, R. B. Hoover, T. W. Barbee and P. F. Boerner, "High resolution imaging with multilayer telescopes: resolution performance of the MSSTA II Telescopes", Opt. Eng. 39(04), 1063-1079 (2000).

[10] S. O. Rice, "Reflection of Electromagnetic Waves from Slightly Rough Surfaces", Commun. Pure Appl. Math., 4, 351 (1951).

[11] J. C. Stover, [Optical Scattering, Measurement and Analysis], 2nd Edition, SPIE Press, Bellingham, WA (1995).

[12] P. Beckmann and A. Spizzichino, [The Scattering of Electromagnetic Waves from Rough Surfaces], Pergamon Press, New York (1963).

[13] J. E. Harvey, [Light-scattering Characteristics of Optical Surfaces], Ph.D. Dissertation, University of Arizona (1976).

[14] J. E. Harvey and R. V. Shack, "Abberations of Diffracted Wave Fields", Appl. Optics 17, 3003 (1978).

[15] J. E. Harvey, "Surface Scatter Phenomena: A Linear, Shift-invariant Process", in [Scatter from Optical Components], J. C. Stover, ed., Proc. SPIE 1165, 87-99 (1989).

[16] J. E. Harvey, C. L. Vernold, A. Krywonos, and P. L. Thompson, "Diffracted Radiance: A Fundamental Quantity in a Non-paraxial Scalar Diffraction Theory", Appl. Opt. 38, 6469-6481 (1999).

[17] J. E. Harvey, C. L. Vernold, A. Krywonos, and P. L. Thompson, "Diffracted Radiance: A Fundamental Quantity in a Non-paraxial Scalar Diffraction Theory: Errata", Appl. Opt. 39, 6374-6375 (2000).

[18] C. L. Vernold and J. E. Harvey, "A Modified Beckmann-Kirchhoff Scattering Theory", Proc. SPIE 3426-05, 51-56 (1998).

[19] J. E. Harvey, A. Krywonos and C. L. Vernold "Modified Beckmann-Kirchhoff Scattering Model for Rough Surfaces with Large Incident and Scattered Angles", Opt. Eng. 46 (7), 078002, 1-10 (2007).

[20] Andrey Krywonos, [Predicting Surface Scatter using a Linear Systems Formulation of Non-paraxial Scalar Diffraction], Ph.D. Dissertation, University of Central Florida (2006).

[21] J. E. Harvey, A. Krywonos, and J. C. Stover "Unified Scatter Model for Rough Surfaces at Large Incident and Scattered Angles", Proc. SPIE 6672, 66720C1-66720C8 (2007).

[22] E. L. Church and P. Z. Takacs, "Instrumental Effects in Surface finish Measurements", Proc. SPIE 1009, 46-55 (1988).

[23] M. G. Dittman, "K-correlation power spectral density & surface scatter model", Proc. SPIE 6291, 62910R1-62910R12 (2006).

[24] J. E. Harvey, Narak Choi, Andrey Krywonos and J. Marcen, "Calculating BRDFs from Surface PSDs for Moderately Rough Surfaces", Proc. SPIE 7426, 74260I1-74260I9 (2009).

[25] J. E. Harvey, A. Krywonos and Dijana Bogunovic, "Non-paraxial Scalar Treatment of Sinusoidal Phase Gratings", JOSA A 23, 858-865 (2006).

[26] A. J. S. Hamilton, "Uncorrelated Modes of Nonlinear Power spectrum", Mon. Not. Roy. Astron. Soc. 312, 257-284 (2000).

[27] A. Krywonos, J. E. Harvey and N. Choi,, "A Linear Systems Formulation of Surface Scatter Theory for Rough Surfaces with Large Incident and Scattering Angles", JOSA A, to be published (2010).

[28] P. Cheimets, D. C. Caldwell, C. Chou, R. Gates, J. Lemen, W. A. Pogorski, C. J. Wolfson, J.-P. Wuelser, "SDO-AIA Telescope Design", Proc. SPIE 7438, 7438G1-7438G12 (2009).

[29] G. Peterson, "Analytic Expressions for In-field Scattered Light Distribution", Proc. SPIE 5178-01, 184-193 (2004).

[30] J. E. Harvey, N. Choi, A. Krywonos, G. Peterson, and M. Bruner, "Image Degradation due to Scattering Effects in Two-mirror Telescopes", Opt. Eng., to be published (2010).

[31] D. Stearns, "Stochastic model for thin film growth and erosion", Appl. Phys. Lett. 62 (15), 1745-1747 (1993).

[32] D. Stearns, D. Gaines, D. Sweeney, E. Gullikson, "Nonspecular x-ray scattering in a multilayer-coated imaging system.", J. Appl. Phys. 84, 1003 (1998).